Complementary acoustic and optical methods for characterization of diffuse venting, gas seeps, and biota distributions at hydrothermal systems: A case study at Kick'em Jenny Volcano, Grenada, West Indies

Eric Mittelstaedt[1*], Clara Smart[2]
[1]Dept. of Geological Science, University of Idaho, Moscow, Idaho, 83843 USA.
[2]Dept. of Ocean Engineering, University of Rhode Island, Narragansett, Rhode Island, USA.
*corresponding author: emittelstaedt@uidaho.edu

ABSTRACT

Quantitatively assessing the impact of hydrothermal circulation on geological and biological systems in submarine environments requires accurate characterization of biota, fluid flow, and, in many shallow systems, gas discharge. In a single vent field, the surface expression of hydrothermal venting and vent biology is often widespread, presenting a significant technical challenge to such characterizations. Typically, attempts to overcome this challenge involve extrapolation of point measurements to estimate field-scale parameters. Extrapolation introduces large uncertainties, however. We present a case study at the Kick'em Jenny Volcano, Grenada, West Indies that jointly applies a set of complementary acoustic and optical measurement methods to significantly reduce uncertainty in field-scale flux estimates of diffuse venting and bubble streams, as well as distributions of biological mats. Two classes of ROV-based methods are used: 1) survey-level techniques for accurately locating fluid and gas discharge across entire vent fields, and 2) local techniques that accurately measure fluid or gas fluxes just above a vent orifice. Survey level techniques included a structured light laser system to locate active diffuse venting and biological mats, and a high-resolution downward facing multibeam system that can resolve individual bubble streams separated by only centimeters. Local techniques included processing of stereo imagery to determine bubble stream parameters (rise rate, bubble size) and application of the Diffuse Flow Velocimetry technique to determine upwelling rates of diffuse effluent. Joint application of these methods provides a several times increase in the number of identified bubble streams relative to ship-board systems and a difference of up to 40 times in field-scale diffuse volume flux estimates relative to currently available techniques.

Keywords: hydrothermal flow, bubbles, seafloor mapping, lasers, classification, diffuse venting
Regional Terms: Lesser Antilles, Grenada, Kick'em Jenny Volcano, 12.30°N 61.64°W

1. INTRODUCTION

Hydrothermal circulation accounts for up to 25% of the Earth's total heat loss through efficient extraction of heat from the crust [*Stein and Stein*, 1994], plays a key role in controlling long-term ocean chemistry [*Elderfield and Schultz*, 1996], and releases significant volumes of mantle volatiles (e.g., CO_2) into the oceans and atmosphere [e.g., *Santana-Casiano et al.*, 2016]. In addition, hydrothermal sites host unique and diverse chemosynthetic biomes [e.g., *Lutz et al.*, 2008; *Nees et al.*, 2008] and can modify local marine ecosystems [*Carey et al.*, 2014b; *Wishner et al.*, 2005]. Quantifying the above local and global impacts of hydrothermal circulation requires vent field-scale characterization of numerous parameters including the distribution of vent biota, as well as detailed and precise flow measurements of fluid and gas discharge. Typically, field-scale estimates of volume flux extrapolate a few point measurements of flow rate to integrate over large spatial areas, a task that is quite difficult to do accurately. Indeed, such integration can be especially difficult when the goal is to incorporate fluxes from several different styles of venting including high-temperature (≥300°C) discrete jets called "smokers" [*Spiess et al.*, 1980; *Von Damm*, 1990; *Von Damm et al.*, 1995] and lower-temperature (≤100°C) diffuse outflows, which are commonly transparent and escape through fractures, porous rock, and sediment [e.g., *Baker et al.*, 1993; *Fisher and Becker*, 1991; *Ramondenc et al.*, 2006; *Trivett and Williams*, 1994; *Von Damm and Lilley*, 2004]. Additionally, many shallow (typically, <1500 m) hydrothermal systems in arc settings exhibit extensive volatile release in the form of bubble streams rising from the seafloor [e.g., *Glasby*, 1971]. Vent sites with widely distributed low-temperature, diffuse flow and/or large numbers of bubble streams in shallow hydrothermal environments present a challenging environment for quantifying fluid and volatile fluxes. Here, we present a new methodology that combines optical and acoustic data sets to decrease uncertainty in field-scale flux estimates for both diffuse flow and gas discharge.

Many previous estimates of diffuse hydrothermal effluent fluxes use visual particle tracking, flow-collector type mechanical/electrical devices, or water column measurements (thermal and chemical) [e.g.., *Baker et al.*, 1993; *Elderfield and Schultz*, 1996; *German et al.*, 2010; *Germanovich et al.*, 2015; *Ginster et al.*, 1994; *Pruis and Johnson*, 2004; *Ramondenc et al.*, 2006; *Rona and Trivett*, 1992; *Schultz et al.*, 1992; *Stein and Fisher*, 2001; *Veirs et al.*, 2006]. In an effort to build upon these methods, development has proceeded on several non-invasive measurement techniques that fall into one of two classes: 1) flow identification and 2) velocity and flux estimates. Methods that identify the spatial extent of diffuse effluent include acoustic [e.g., *Rona et al.*, 1997] or structured light techniques [*Smart et al.,* 2017*; Smart et al.,* 2013]. These methods precisely identify the locations of active diffuse venting, but cannot currently determine flow rates. In contrast, non-invasive methods that use image processing techniques to track refractive index anomalies (parcels of hot or saline fluids) can locally estimate diffuse effluent velocities or fluxes. Examples of methods that estimate fluid velocities include Diffuse Flow Velocimetry (DFV) [*Mittelstaedt et al.*, 2010], and a laboratory developed method relating the frequency and velocity of refractive index perturbations in the water column to the thermal characteristics of fluid flux [*Barreyre et al.*, 2015]. Although both these techniques estimate flow rates, measurements encompass small areas, making estimation of fluid fluxes across an entire vent field difficult without other constraints. To date, the above two classes of measurement techniques have not been used cooperatively; a key focus of this study.

Due to time constraints during field surveys, locating and collecting direct measurements of flow rates at every location where diffuse effluent rises from the seafloor is impractical with available technology. To circumvent this limitation, studies often extrapolate point measurements to the scale of an entire vent field [e.g., *Rona and Trivett*, 1992]. Recently, field-scale extrapolation has been improved by the use of seafloor photo mosaics [e.g., *Barreyre et al.*, 2012; *Escartin et al.*, 2015; *Mittelstaedt et al.*, 2016]. Extrapolation of point measurements using photo mosaics is performed by multiplying locally measured flow rates by the total area covered by white microbial mats. Limiting the extrapolation to areas with identified microbial mats (likely to host active diffuse outflow) improves flux estimates by reducing uncertainty in the areal extent of active venting. However, microbial mats often exist in locations with low or no obvious fluid flow. For instance, the extensive seep site detailed in *Carey et al.* [2014a] was characterized by microbial mats and biota, however, no active fluid flow was observed during extensive exploration. Thus, despite improving on previous methods, uncertainties in flux estimates based on photo mosaics are potentially quite large.

Similarly, methods to estimate the gas flux from bubble streams employ both high-altitude (acoustics) and local (acoustic and optical) methods to locate and analyze rising bubble streams at active seeps. Large differences in acoustic impedance associated with rising gas bubbles yield strong signals in multibeam sonar water column data. These strong sonar reflections have been extensively used to locate active seeps and to quantify the distribution of rising bubbles [*Merewether et al.*, 1985; *Schneider von Deimling and Papenberg*, 2012; *Skarke et al.*, 2014; *Weber et al.*, 2012]. Software packages, such as FFMidwater, analyze multibeam water column data and allow for automated detection of rising bubbles within the water column [*Fledermaus*, 2014; *Urban et al.*, 2017]. However, although the majority of these approaches use a modern, ship-board multibeam system (e.g., a Kongsberg EM302), sensor limitations preclude differentiating between bubble stream sources separated by less than a meter. Conversely, mounting a downward looking high-resolution multibeam sonar system on a remotely operated vehicle (ROV) provides data similar to shipboard multibeam data, although at a resolution on the order of centimeters [*Roman et al.*, 2012].

Local optical and acoustic imaging of bubbles can supplement multibeam studies by quantifying the fluxes of escaping gases. For example, a forward looking ROV-mounted sonar system can be used to discover new locations and the rise rates of methane bubbles within the water column [*Socolofsky et al.*, 2015; *Wang et al.*, 2016]. Indeed, with an appropriately calibrated, forward looking system, the flux of a particular bubble stream can be determined [*Nikolovska et al.*, 2008]. Similarly, stereo imagery combined with automated detection methods allows tracking and size estimates of bubbles, providing an alternate method for estimating gas flux from bubble seeps [*Wang and Socolofsky*, 2015]. However, many of these methods require specifically designed and calibrated sensors, increasing sampling costs, and requiring specific vehicle platforms.

Observations and analysis show that vent fauna are very sensitive to the chemical and thermal flux of vent fluids and the degree of mixing with oxygen-rich seawater [*Moore et al.*, 2009; *Schmidt et al.*, 2008; *Stewart et al.*, 2005]. Thus, in conjunction with measurements of effluent fluxes, characterization of biota distributions can provide important constraints on the relationship between venting and biology at hydrothermal systems. Quantitative estimates of biota distributions can face many of the same difficulties as fluid flux measurements: 1) biota density varies significantly over a vent field, 2) measurements of biota distributions in the field require time-consuming, detailed surveys, and 3) relying on spot measurements alone introduces large uncertainties. Accurate and rapid characterization requires automated, detailed methods for characterizing seafloor data including photo mosaics and structured light imaging [e.g., *Barreyre et al.*, 2012; *Smart et al.*, 1979.].

In this paper, we present a comprehensive suite of measurement techniques, which: significantly reduce the uncertainty in field-scale diffuse flux estimates, improve the location resolution of bubble streams, and provide an automated technique for quantifying the distribution of biota and active diffuse venting. The techniques we present rely on recent developments in non-invasive imaging techniques, high-resolution ROV-mounted sonars, relatively low-cost computer vision cameras, and structured light imaging. Using these methods together, data collection on the scale of a vent-field can be achieved in a relatively small number of ROV dives. We present an illustrative case study using these complementary acoustic-optical methods at two vents in the inner crater of the Kick'em Jenny Volcano: Shrimp Vent and Champagne Vent. The vents of Kick'em Jenny provide a useful testing ground as they host both diffuse venting and extensive gas release in the form of bubble streams. Our results indicate that a joint approach whereby methods that precisely identify the location of active outflow (bubbles or diffuse effluent) and biota are coupled with local methods that measure fluid and gas emissions yields better estimates of total flux and biology-vent interactions than possible using these methods separately. Collecting co-registered, comprehensive, high-resolution imaging data sets alongside fundamental *in-situ* sensor data has the ability to efficiently characterize hydrothermal and seep activity while identifying associated biota and geologic features.

2. KICK'EM JENNY VOLCANO

Kick'em Jenny is a submarine volcano located 7.5 km northwest of Grenada in the southern Lesser Antilles Arc (Figure 1). The volcanic edifice has a diameter of ~5 km at its base and rises 1300 m from the seafloor to its summit at a depth of 180 m. The summit region hosts a ~100 m deep outer crater that recently dropped by ~18 m following an eruption in 2001 [*Watlington et al.*, 2002], as well as a smaller, several meter deep inner crater. Kick'em Jenny is the only known active submarine volcano within the Lesser Antilles Arc and is currently the most active volcano with 12 eruptions since 1939 [*Devine and Sigurdsson*, 1995; *Lindsay et al.*, 2005; *Watlington et al.*, 2002]. Eruptions at Kick'em Jenny manifest as either explosive, tephra-producing or non-explosive, dome-forming events [*Devine and Sigurdsson*, 1995].

Hydrothermal activity at Kick'em Jenny is observed on the volcano flanks [*Koschinsky et al.,* 2007] and within the outer and inner craters [*Carey et al.*, 2014b; *Carey et al.*, 2016; *Graff et al.*, 2008]. Most hydrothermal activity occurs within the inner crater where observations find high-temperature fluids up to 270°C, lower temperature (~14-17°C) diffuse fluids venting through fissures and cracks, and gas venting in the form of bubble streams taken as an indication of subsurface phase separation [*Graff et al.*, 2008]. Large areas of the inner crater floor are covered by reddish-orange iron oxides associated with low-temperature diffuse flow; white to gray microbial mats are observed around some vents (Figure 2). The highest temperature vents cluster along the margins of the inner crater and at small mounds on the crater floor [*Carey et al.*, 2014b]. This study focuses on two of the largest vents, the Champagne and Shrimp Vents, which host both bubble streams and diffuse venting (Figure 3).

Previous observations have characterized the areas of venting and fluid temperatures at Shrimp and Champagne vents [*Carey et al.*, 2016; *Smart et al.*, 1979.]. The area surrounding Shrimp Vent hosts low temperature discrete and diffuse venting and hundreds of bubble streams exiting the seafloor on a steep hillside. Biological activity includes white microbial mats, dark bacteria within the flocculent orange sediment, and red shrimp (*Alvinocaris sp.*) observed living in crevices and below rocks in the presence of low temperate diffuse venting. Fluid temperatures reach up to 180°C [*Carey et al.*, 2016], but are commonly closer to 35°C. The second area of interest, the Champagne Vent, is defined by a ~1 m diameter, ~0.5 m high mound from which numerous bubble streams emanate and sparse diffuse flow is observed. The bubble discharge rate differs significantly across the mound surface. Areas of white bacteria are present, but no shrimp were observed during our exploration of Champagne. When disturbed, the surrounding seafloor is light in color and highly reflective, suggesting the presence of microbial communities within the sediment. Fluid temperatures reach up to 160ºC in the central orifice of Champagne Vent [*Carey et al.*, 2016].

3. DATA

In September and October 2014, E/V *Nautilus* undertook an exploration and measurement campaign (Cruise number NA054) at Kick'em Jenny Volcano using the remotely operated vehicle (ROV) *Hercules*. *Nautilus* previously visited Kick'em Jenny in 2013 [*Carey et* *al.*, 2015]. We present results from high resolution imaging and sampling efforts conducted within the inner crater at the Shrimp and Champagne vents during both research cruises.

3.1 Data Collection by Telepresence

The E/V *Nautilus* is telepresence enabled, allowing shore-based scientists to observe exploration actives in real time and communicate directly with ship-board engineers and scientists [*Bell et al.*, 2016]. Cruise NA054 was part of the *Transforming Remotely Conducted Research through Ethnography, Education, and Rapidly Evolving Technologies* (TREET) project funded by the National Science Foundation INSPIRE program with the goal of evaluating the potential for telepresence-enabled marine science [*Bell et al.*, 2015]. TREET used telepresence to bring together teams of researchers and students from multiple institutions to direct data and sample collection and to evaluate real time results throughout the sea-going expedition. During NA054, scientists and engineers aboard E/V *Nautilus* worked with shore-based participants to determine potential areas of mapping and sampling; shore-based scientists and students then directed sampling efforts with the ROV *Hercules*. Input from multiple lead scientists allowed for the collection of comprehensive data sets, including bubble and flow imaging, high resolution mapping, and *in-situ* sampling at both the Shrimp and Champagne vents.

3.2 High-Resolution Imaging and Survey Methodology

The ROV *Hercules* is equipped with a pair of forward looking stereo cameras and a high-resolution downward looking imaging suite capable of collecting optical and acoustic data at centimeter-scale resolution. The forward looking stereo cameras include a pair of mono computer vision cameras mounted on a fixed bracket with a baseline of approximately 10 cm on the ‘front porch’ of the vehicle. Each camera has a 30° by 40° field of view, a 1388x1038 resolution, records imagery at 10-12 Hz, and is focused and calibrated for imaging objects between 0.5 m and 1.5 m away. The stereo cameras were used to collect imagery of both diffuse flow and bubble streams for local analysis of rise rates, bubble sizes, and fluid velocities (Section 4; Figure 4). During acquisition, one of two image backgrounds (31 cm x 55.5 cm white for bubble imaging, or 34.3 cm x 47 cm speckled for DFV) was placed behind the rising effluent or bubbles, isolating the area of interest. To provide a steady imaging platform, the ROV rested upon the seafloor during collection of bubble or diffuse flow imagery.

The downward looking, high-resolution imaging suite is mounted on the back of the ROV *Hercules* away from the forward operational lights (Figure 5) [*Roman et al.*, 2012]. The system includes a pair of stereo cameras (12-bit 1360 x 1024 pixel Prosilica GC1380 computer vision cameras), one color and one mono, each with a 30° x 40° field of view in water, as well as a structured light laser system consisting of a third (12-bit mono Prosilica) camera and a verged 100 mW 532 nm green sheet laser (manufactured by Coherent Powerline) mounted on a rigid frame with known relative geometry. Downward looking stereo imagery was used to create seafloor photo mosaics, while the structured light system collected images of the laser line along the seafloor to determine sub-centimeter bathymetry, optical backscatter, seafloor classification, and to detect active diffuse venting [*Inglis et al.*, 2012; *Smart et al.*, 1979.; *Smart et al.*, 2013]. Finally, the suite also includes a downward looking 1350 kHz multibeam sonar system designed by BlueView Technologies, which collected water column data at an altitude of ~3 m above the seafloor to identify and locate bubble streams.

Simultaneous collection of optical and acoustic data by the downward-looking high resolution imaging suite occurred in pre-determined survey patterns over several dives. (Figure 6). During each survey, ROV *Hercules* maintained a 3 m altitude and a horizontal velocity of 0.18 m s^{-1}. Tracklines extended up to 50 m in length with an across track spacing of 1.2-1.7 meters allowing for > 20% across track sensor overlap. To ensure centimeter-scale resolution, data collection rates were 20 Hz for laser imaging, 15 Hz for multibeam, and 0.33 Hz for the stereo cameras.

The primary navigation sensor used during each survey was a Doppler velocity log (DVL), which determines current position based on the previous position and integrated vehicle velocities based on bottom tracking. For NA045, the DVL operated at 600 kHz in bottom tracking mode. Over the period of a single survey, cumulative error can result in drift of DVL relative navigation values on the order of tens of centimeters. DVL drift is corrected by regular resetting of the DVL position with the Ultra Short Baseline (USBL) sensor system (TrackLink 5000MA system manufactured by LinkQuest), which has a stated accuracy of one degree, equivalent to errors of < 2% of vehicle depth. However, within the crater of Kick'em Jenny acoustic propagation errors occurred due to variations in fluid density stratification, and reflections off the steep crater walls, which yielded errors up to 5% of water depth. Therefore, absolute navigation error up to 15 meters within the data presented in this study are not uncommon. To correct for absolute location errors, we used visual markers on the seafloor that were observed in stereo images (downward looking cameras) and co-registered with vehicle navigation (DVL and USBL), multibeam sonar, and laser data. After processing of the navigation data, we estimate maximum cumulative intra-survey navigation errors up to a few centimeters and absolute location error of each set of survey lines up to ~1 m.

3.3 Bubble Trap

To quantify gas flux rates from bubble streams, we attached a 35 cm diameter, two-liter pitcher with volumetric markings to the arm of the ROV *Hercules* (Figure 7). The pitcher was placed upside down over an active bubble stream and the time required for the rising gas bubbles to displace two liters of water was recorded three times at each sample site (Table 1). Observations were recorded by the forward-looking HD camera on *Hercules*. Bubble flux measurements were performed at four sites in total with two distinct sites near each of the Shrimp and Champagne Vents, providing 12 independent flux measurements. This capture method is similar to that employed successfully by *Nikolovska et al.* [2008].

3.4 Temperature Measurements

Measurements of diffuse fluid temperatures were collected using the Woods Hole Oceanographic Institution High-Temperature Probe onboard *Hercules*. Temperatures were recorded near the seafloor and in the water column, just beneath the field of view of the forward looking stereo cameras. Measurements were typically conducted during collection of flow imagery used for DFV. We report mean temperature values here (Table 3).

4. METHODS

4.1 Diffuse Flow Velocimetry

The DFV method is detailed in *Mittelstaedt et al.* [2010], but a brief summary is presented here. DFV uses a series of video images of a motionless, random dot pattern as viewed through the lens of a moving refraction index anomaly (e.g., a hot upwelling fluid passing through ambient seawater). When viewed in two sequential images, the background dot pattern appears to deform due to movement of the refraction index anomaly, changing the pattern of apparent distortion in the image. Movement of the refraction index anomaly will cause the apparent distortion to move across the image at the rate of fluid flow. Over short time periods (<~1 s) the pattern of deformation remains unchanged and can be tracked using cross-correlation techniques. The two-step DFV calculation first determines the change in apparent deformation between sequential background images and then tracks movement of the apparent deformation pattern (between these deformation calculations) to estimate fluid velocities.

In the first step of the DFV method, the deformation field is determined using a multi-level Particle Image Velocimetry (PIV) algorithm [e.g., *Westerweel*, 1997; *Willert and Gharib*, 1991]. Particle Image Velocimetry divides images into a grid of overlapping windows (Table 2). A succession of window sizes is utilized from 32x32 pixels to 8x8 pixels, each with an overlap of 50%. Using Fourier convolution, intensities of the pixels within each window are cross-correlated with intensities in the subsequent image. The location of the maximum correlation corresponds to the highest probability displacement of the window caused by a change in the apparent deformation pattern. Repetition of this calculation across all pixel windows in an image produces an instantaneous 2D vector field of the apparent background deformation due to movement of the index of refraction anomaly between two images.

The second step of a DFV calculation tracks the pattern of apparent background deformation vectors as they move with the fluid between PIV calculations. Similar to the PIV calculation, two sequential deformation vector fields are divided into overlapping windows of vectors. A single window size (32x32 to 16x16 vectors, depending upon the flow) was used with a 50% overlap (Table 2). For each window, the X and Y components of each apparent deformation vector are cross-correlated to determine the highest likelihood shift of the vector window, thus giving the shift associated with fluid motion in the time between two calculations (e.g. approximate fluid velocity). The precision of the location of the correlation minimum is improved from ±0.5 times the distance between vector locations to ~±0.1 times the inter-vector distance with an analytical 3-point Gaussian fit in both coordinate directions [*Willert and Gharib*, 1991]. This calculation is performed on all the vector windows to yield the instantaneous, 2D velocity field.

The location of the maximum correlation gives the highest probability displacement of the deformation field in the window, but outliers can occur due to poor image quality, little or no fluid movement, and/or undetectable deformation (due to very small, very large, or nonexistent density variations). Two methods are used to limit false correlations. First, the velocity is considered valid only if the curvature of the correlation peak in the immediate neighborhood of the correlation maximum is greater than an empirically determined critical value between $1x10^{-7}$ and $1x10^{-5}$. Second, a window shift is considered invalid if it falls on the boundary of the correlation matrix. If a given shift fails these tests, it is assumed to be erroneous and the velocity in that location is set to 0.

Particulate matter in the water is another potential source of error during DFV processing. During deployment of the background board by the ROV *Hercules*, low densities of particulate matter were observed within the upwelling diffuse effluent between the camera and the background. Higher concentrations of particles can decrease the quality of DFV calculations, but this is not always the case. In general, floating particles yield one of two effects: 1) the correlation peak near the particle is poor and the value is thrown out (as described above), or 2) the calculation treats the particle motion as apparent deformation and will follow this 'deformation' across two calculations yielding the velocity of the particle, which should be similar to the fluid velocity. Each individual particle only interferes with a single velocity vector calculation, limiting their impact on flow calculations when the particle density is low. Yet, even in the case where numerous particles are present in an image, the velocity field will still represent the motion of the fluids and/or vectors will be removed where poor correlations occur. Thus, particulate matter is likely to have a small impact on DFV calculations.

When using DFV to estimate diffuse effluent volume flux, care must be taken to account for entrainment of ambient seawater by buoyantly upwelling diffuse fluids. DFV calculates fluid velocities at a height above the fluid exit orifice that is a function of the height of the background board. In the measurements presented here, the DFV image background was placed directly on the seafloor (e.g., Figure 4D) for all, but one measurement sequence (survey 1928, Table 2) yielding average heights of velocity calculations of ~15 cm (~45 cm for survey 1928). If we make the first order assumption that entrainment processes can be described using the theory for pure plumes [*Fischer et al.,* 1979] or buoyant jets [e.g., *Morton et al.,* 1956], we can estimate the ratio of volume fluxes calculated at the height of DFV measurements and the vent orifices. The pure plume (i.e., no initial volume or momentum flux) model for a circular orifice (roughly applicable for our measurements), yields a source volume flux Q_0 equal to the source buoyancy flux B divided by the thermal expansivity β (2.78 x 10^{-4} °C^{-1}) multiplied by the temperature anomaly ΔT and the acceleration of gravity g (9.81 m s^{-2}), where $B = z(u_c/4.7)^3$, and u_c is the centerline velocity estimated from DFV [*Fischer et al.,* 1979]. The volume flux at a height z above the orifice is given by $Q = \pi(0.1z)^2 u_c$, where $r = 0.1z$ approximates the plume radius [*Fischer et al.,* 1979]. Thus, the ratio of Q to Q0 is

$$\frac{Q}{Q_0} = \frac{1.04\beta\Delta T g\pi z}{{u_c}^2}. \qquad (1)$$

In the case of a buoyant jet, buoyancy flux is approximately constant with height above the orifice [*Morton et al.*, 1956]. Thus, the ratio of the source volume flux to that measured at a height z is a function of ΔT at each height,

$$\frac{Q}{Q_0} = \frac{B/\beta\Delta T_z g}{B/\beta\Delta T_S g} = \frac{\Delta T_S}{\Delta T_z}, \qquad (2)$$

where subscripts s and z indicated temperature anomalies measured at the orifice height and the measurement height, respectively. We estimate the impact of entrainment on our calculated volume fluxes after we present results for fluid velocities and temperatures (see Section 6.1.2).

4.2. Structured Light Identification of Diffuse Outflow

Structured light laser sensors are sensitive to changes in bathymetry, seafloor character, and turbulent fluid density anomalies. Sensitivity to these phenomena allow detection of areas of diffuse hydrothermal flow and biota, as well as sub-centimeter bathymetry [*Smart et al.*, 2017; *Smart et al.*, 2013]. In the presence of turbulent fluid density anomalies, a laser line is diffracted and appears blurred instead of crisp (Figure 8). Computationally, the spread of the laser line is indicated by the intensity weighted second moment about the peak intensity of the laser line. In the presence of active fluid flow, the value of the second moment increases and the optical intensity of the laser line decreases. In contrast, increasing optical intensity values alongside minimal changes in the intensity-weighted second moment indicate changes in seafloor type and can correspond to the presence of microbial mats. A machine classification routine considers the intensity weighted second moment and optical intensity values to differentiate between active fluid flow, bacteria, and plain seafloor (Figure 9). Using the collected structured light data, we generate geo-referenced maps of bathymetry, optical intensity, areas of active venting, and a classification of the seafloor.

The primary sources of noise in this structured light system involve disturbances of the seafloor. Trash on the seafloor and sediment clouds caused by fish motions can result in false classification of active venting. Bacteria can also occasionally be classified as active venting. To limit these errors, corresponding imagery and ground truth observation is valuable and commonly collected simultaneously with laser data. Overall, however, this system robustly distinguishes between areas of plain seafloor and areas of interest. For detailed error metrics, see *Smart et al.,* [2017].

4.3 Multibeam Bubble Stream Identification

Bubbles were located within the downward looking BlueView multibeam sonar water column data (Section 3.2). For the illustrative purposes of our relatively small surveys, the bubble detection scheme was not automated, rather, rising bubble streams were identified manually within water column images (Figure 10A). Each water column image was converted to an individual tiff with an associated timestamp and location. The lateral location of bubble streams in each tiff were identified using the ginput function of Matab© and converted to X and Y locations using the heading and location of ROV *Hercules* from the DVL navigation. Final locations of individual bubble streams were determined by assuming that points located within 30 cm across- and 5 cm along-track distance denoted a single bubble stream (Figure 10B,C). We used a larger across-track distance to compensate for DVL drift (Section 3.2).

4.4 Bubble Rise Rates and Size Distributions

We collected stereo images of bubbles rising from seep sources at 10-12Hz. From these images, we estimate bubble rise rate and bubble size distribution. Rise rate is determined by identifying common bubbles in images sequentially spaced 1-3 frames apart, from a single camera. The elapsed time between images and the difference in vertical position of each bubble yielded the rise rate in pixels per centimeter. The stereo calibration then allowed rise rates to be converted to millimeters per second. Individual bubble sizes were determined manually by measuring the diameters of bubbles within each image of a stereo pair. These measurements were then converted to volumes by assuming spherical bubbles; the assumption of spherical bubbles was chosen for simplicity. While image processing algorithms differentiating the bubble from the background would allow for automated size estimates (e.g., non-spherical bubbles), rise rates, and bubbles fluxes, this approach was determined to be unrealistic in this study due to lighting conditions such as shadows from rising bubbles and the reflective nature of the white background used in this study. Thus, automated methods could not reliably be used to identify and separate out image characteristics of the rising bubbles. To facilitate flux estimates in future studies, the background color (black or white) and lighting conditions (e.g., side lighting) should be designed to minimize the difficulties described above and to allow for automated methods.

5. RESULTS

5.1 Diffuse Flow Locations and Flux Estimates

5.1.1 Locations of Active Diffuse Flow

Seafloor classification results from the structured light laser sensor indicate areas of plain seafloor, bacteria, and active fluid flow. Due to differences in data quality, we use results from surveys conducted in 2013 at Shrimp Vent and in 2014 at Champagne Vent. Changes in vent structures were not notable between surveys in these two years. Collected laser line data followed the processes outlined in *Smart et al.,* [2017] and was intensity normalized based on range and acquisition parameters before being passed through the support vector machine classification algorithm. Data were gridded at 0.5 cm resolution to ensure proper identification of small areas of diffuse venting, often only a few centimeters across. For illustrative purposes, seafloor classification data is shown for small areas (~10's of square meters) where sampling occurred at the vent sites, as well as a 15x5m section of the Shrimp Vent area to illustrate scalability of the method (Figure 11A-C).

Within the Shrimp Vent survey, active flow was restricted to small discrete fluid density anomalies indicating hydrothermal discharge at a low volume flux. The majority of fluid flow was detected within larger microbial mats or alongside small rocky features. These results align with observations made using the ROV mounted HD camera indicating that venting is dominated by rising bubble streams (Figure 2A), while active fluid flow is sparse and often identified following the observation of shrimp. Significant microbial mats are also detected by the structured light system and are verified by photo mosaic imagery (Figure 9A, Figure 11A-C). Champagne Vent is significantly smaller in area than Shrimp Vent and the majority of hydrothermal activity is located around the main mound described in Section 2. As at Shrimp Vent, gas bubbles dominate this site, however, significant diffuse flow was also detected and confirmed during sampling efforts (Figure 11D-F). Error within this survey is apparent in the detected fluid flow south of the mound which is a false positive result caused by disturbance of fine sediment by the fish apparent in the mosaic. While this area does not contain the extensive white microbial mats apparent within the Shrimp Vent images, significant bacteria is detected. As previously noted, disturbance of the sediment, apparent where the ROV landed during sampling activities, reveals bright areas of sediment, that likely contain bacteria. The presence of bacteria within the sediment, rather than white microbial mats, is likely responsible for the bacteria detection results within the resulting classification figures. Distinct areas of diffuse flow from both sites were also imaged using the forward looking stereo cameras for DFV measurements.

5.2.2 Local Measurements of Diffuse Volume Flux

DFV measurements were performed on six image sequences captured at 10 Hz spanning periods of 10 s to 400 s with a mean sequence length of 266.5 s. Chosen sequences had little to no ROV motion, low particle concentrations, and a lack of fauna, sensors, or other objects in the camera field of view. As commonly observed in diffuse flow [e.g., *Mittelstaedt et al.,* 2012; 2016], fluid velocities exhibit rapid, small-scale variations in direction and magnitude. However, a preferred flow direction was observed in each image sequence. To assess the time variability and the average flux within each image sequence, we calculated the spatial median value in each DFV calculation and the overall mean and standard deviation of these spatial medians (Figure 12 and Supplementary Figures S1-S5, Table 3). The measured vertical component of flow ranged from 0.3 cm s^{-1} to 2.52 cm s^{-1} for fluid temperatures between 16.6°C and 50.8°C (Table 3). Median vertical velocities show an approximately linear dependence on the square-root of fluid temperature anomalies (ambient temperature in the inner crater is ~14.8°C), similar to predictions for buoyant, turbulent jets [*Morton et al.*, 1956] (Figure 13). Lateral velocities have similar magnitudes to the measured vertical velocities with relatively steady flow in most image sequences (Figure 12 and Supplementary Figures S1-S5). Changes in the lateral component of flow between image sequences indicated changes in the circulation pattern of water within the Kick'em Jenny crater, but the number and length of measurements was insufficient to meaningfully quantify these changes.

5.2 Bubble Locations, Rise Rates, Sizes and Gas Fluxes

In total, we identified 1683 individual bubble streams in the areas around the Champagne and Shrimp vent sites. Most bubble streams (1274) were located near the Shrimp Vent with a maximum bubble stream density of 56 streams per m^2 (Figure 10). Video observations suggest that bubble streams at Shrimp Vent have similar discharge rates across a broad area. At Champagne Vent, there are two distinct areas of gas discharge separated by a ~8 m wide area with no identified bubble streams. Champagne Vent hosts 409 bubble streams with bubble discharge across a smaller total area than Shrimp Vent. Bubble stream densities are lower and the maximum density is smaller (37 streams per m^2). In contrast to Shrimp Vent, video observations show a large difference in bubble stream fluxes between a large central bubble stream and numerous smaller seeps surrounding the main Champagne bubble seep (Figure 7A).

Bubble rise rates were determined for >5000 individual bubbles in stereo imagery. Rise rates show an approximately normal distribution (Figure 14A) with most rise rates between 20 cm s^{-1} and 60 cm s^{-1}. In addition to rise rates, we measure individual bubble sizes on a subset (n=170) of these bubbles. Measured bubble diameters range from 1.8 mm to 9.8 mm with a mean of 4.8 mm. Assuming spherical bubbles these measurements yield bubble volumes of between ~27 mm^3 and ~4000 mm^3. Although there is significant scatter for small bubbles, bubble rise rates generally decreased with increasing bubble size (Figure 14B).

Gas discharge rates were measured at 4 different seep sites, each with 3 repeat measurements. Discharge rates ranged from 0.171 liters/min to 2.03 liter/min. Repeat measurements at each seep varied by 1.5% - 12% suggesting that fluxes are steady over at least periods of minutes to hours. The largest measured flux rate was observed at the main bubble seep of the Champagne Vent.

5.3 Integrated Fluid and Gas Fluxes from the Champagne and Shrimp Vents

5.3.1 Champagne Vent

Fluid fluxes in the Champagne vent area are based upon DFV measurements and the classification of structured light imaging over a survey area 10.6 m long and 7 m wide (74.2 m^2). Combining classification results (1.03 m^2 active venting) with the temporal average of spatial median vertical fluid velocities from DFV measurements in the Champagne vent area (1.2 ± 0.67 cm s^{-1}; Table 3) yields a diffuse volume flux of 10,610 ± 6,900 cm^3 s^{-1} with errors defined by the standard deviation in DFV measured flow rates. If we assume that areas of microbial mats (30.41 m^2) represent active fluid flow, our total diffuse flux estimate would be ~30 times larger at 313,200 ± 203,750 $cm^3\ s^{-1}$.

We calculated the total gas output of the Champagne Vent area by assuming that the flux measured at the main gas seep on top of the primary mound (Champagne Vent 2: 33.48 ± 0.31 $cm^3\ s^{-1}$) is significantly larger than all surrounding vents identified in the BlueView multibeam sonar water column data. For the surrounding seeps (N=409), we assumed fluxes equal to Champagne Vent 1 (2.92 ± 0.07 $cm^3\ s^{-1}$; Table 1). ROV video observations support this assumption (Figure 7A); bubble discharge was much more vigorous from the seep atop the Champagne mound than elsewhere. Thus, we estimate a gas flux from the Champagne Vent area of (33.48 ± 0.31 $cm^3\ s^{-1}$ + 409 x 2.92 ± 0.07 $cm^3\ s^{-1}$) 1227.7 ± 28.9 $cm^3\ s^{-1}$.

5.3.2 Shrimp Vent

Fluid fluxes in the Shrimp vent area are based upon DFV measurements and classification of structured light imaging over a survey area 31.4 m long and 7.1 m wide (222.3 m^2; Supplementary Figure S6). Combining classification results (0.35 m^2 active venting) with the temporal average of spatial median vertical fluid velocities from DFV measurements in the Shrimp vent area (0.3 ± 0.26 $cm\ s^{-1}$) yields a diffuse volume flux of 1050 ± 910 $cm^3\ s^{-1}$ with errors defined by the standard deviation in DFV measured flow rates. If we make the assumption that areas classified as microbial mats (14.8 m^2) represent areas of active fluid flow, we would calculate a total diffuse flux of 44,400 ± 38,500 $cm^3\ s^{-1}$, >44 times the estimate based upon the structured light classification. Although some flow is likely obscured by rocks or is too faint to detect with the structured light system, the uncertainty on active flow area is small relative to the difference between areas of active flow and areas of microbial mats.

Gas fluxes measured around Shrimp Vent showed approximately constant rates across six measurements at two sites (Table 1). Observations using ROV video support similar gas discharge at seeps across the Shrimp Vent area. Thus, to estimate a total gas flux from Shrimp Vent, we multiply the mean measured seep flux (7.6 ± 0.44 $cm^3\ s^{-1}$) by the number of identified bubble streams (1274), yielding a total gas discharge rate of 9680 ± 560 $cm^3\ s^{-1}$.

6. DISCUSSION

6.1 Limitations of the Available Kick'em Jenny Dataset

6.1.1 Spatial Limitations

The focus of this study is to demonstrate synergy between several measurement techniques for characterization of diffuse flow and gas seeps, not to provide comprehensive flux measurements from the Kick'em Jenny Volcano. The principle focus of the 2013 and 2014 studies at Kick'em Jenny was exploration and sampling with supplementary flux measurements using a suite of non-invasive instruments. Thus, limited ROV time was available for flux measurements, and they do not span the entire inner crater. Despite these limitations, the data set is sufficient to demonstrate how coordinated use of optical and acoustic methods can decrease uncertainty in flux estimates for diffuse flow and gas discharge.

6.1.2 Impact of Entrainment on Volume Flux Measurements

Entrainment of ambient seawater into rising diffuse fluids causes effluent volume flux to increase with height above the source. With increasing height above the seafloor, entrainment decreases fluid vertical velocity (measured by DFV) and temperature and increases upwelling width (imaged by structured light methods). Using a pure plume or buoyant jet model, we can estimate the ratio of the volume flux at the height where the areal distribution of diffuse outflow is measured to the volume flux at the vent orifice. For the purpose of this discussion, we assume that structured light imaging measures the area of active diffuse flow at a height above the seafloor equivalent to the height of DFV measurements (~15 cm for all surveys except survey 1928, which was at 45 cm). In these calculations, centerline plume velocities are estimated as the mean DFV velocity plus the standard deviation. For the case of a pure plume model (Equation 1), we calculate values of Q/Q_0 = 35-77. For the buoyant jet model, Q/Q0 varies between 2.5 for survey 2340 and 20 for survey 1829 (the only surveys where temperatures were measured at both the DFV measurement height and at the orifices). As the diffuse flows imaged here act as buoyant jets, not pure plumes, our estimates for total volume fluxes from Champagne and Shrimp vents maybe overestimated by ~2.5 - 20 times. Note, however, that this correction for entrainment does not affect the differences in volume flux measurements between structured light imagery and photo mosaics discussed below; future surveys focused on quantifying total volume fluxes should carefully account for entrainment in their estimates.

6.2 Benefits of Complementary Measurement Methods

6.2.1. Diffuse Venting

When implemented independently, the techniques used in this study either effectively locate active diffuse venting across wide areas or measure upwelling rates of diffuse effluent at one vent, but cannot separately achieve both tasks. For example, a flux measurement using the DFV method requires accurate placement of an ROV followed by image capture at a single vent spanning a duration of ~1-10 minutes. Depending upon the goals of a seagoing expedition, it might be impractical to perform a comprehensive suite of DFV diffuse flow measurements, making extrapolation necessary. In contrast, structured light imaging identifies the spatial distribution of diffuse flow and microbial mats across a relatively large area in a few hours through an ROV survey at ~3 m altitude. However, structured light imaging cannot measure diffuse flow rates. Combining these methods yields an improved flux estimate by taking key sets of precise measurements using DFV and coupling them with accurate locations of active diffuse flow across the study area.

Several studies attempt to extrapolate point source measurements of diffuse flow using photo mosaics of the vent field [e.g., *Barreyre et al.,* 2012; *Mittelstaedt et al.,* 2016]. Although photo mosaics provide a powerful tool for placing vents in their geologic context and mapping the distribution of various flora and fauna, including white microbial mats, they cannot be used to identify areas of active diffuse venting. To overcome the inability to identify active outflow, studies using photo mosaics to estimate total vent field fluid flow often rely on white microbial mats to indicate areas of active venting. The structured light system, however, detects specific areas of turbulent density anomalies (active flow), which rarely span the full extent of white microbial mats. Our flux estimates for the Shrimp and Champagne vent areas demonstrate that estimates using microbial mats versus mapped areas of active venting can differ by 30-50 times at Kick'em Jenny. In fact, the majority of observed venting within the Shrimp Vent area was not located within patches of bacteria at all, rather, it was found emanating from cracks, or around rocks. Without visually locating shrimp (cm in length) hiding under rocks within the photo mosaic, there would be no indication of hydrothermal activity. Additionally, while considering the distribution of microbes, only large microbial mats are observable within a mosaic causing microbial life within the sediment to be ignored, as demonstrated by the Champagne Vent survey.

Potential benefits of joint DFV and structured light methods also extend to field logistics including operations schedules, the use of telepresence, and efficient use of ROV bottom time. Both systems are vehicle agnostic; the structured light system can be mounted on most ROVs and on AUVs such as *Sentry*, and the DFV system can be run on most ROVs or Human Operated Vehicles (HOV) such as *Alvin*. This flexibility suggests a possible field scenario of nighttime AUV-based structured light mapping and daytime HOV-based DFV measurements. On-shore scientists can also use telepresence to direct both DFV measurements and structured light mapping; in fact, many of the DFV measurements for this study were directed from shore by the lead author. Finally, by conducting an initial survey using the structured light system over an area of interest, sampling locations and DFV measurement sites can be identified prior to deploying an ROV for *in-situ* measurements at specific vents. Pre-dive knowledge of active vent locations will improve efficiency and avoid missing key locations of active venting or microbial populations that were not directly observed during ROV operations.

6.2.2 Bubble Streams

Our framework for bubble stream identification, and bubble rise rates and sizes uses a combination of local video imagery combined with remote location determinations from high-resolution multibeam sonar water column data. This coupled methodology provides similar benefits to combining structured light and DFV measurements for diffuse flow: 1) high-resolution ROV bubble stream identification improves spatial resolution of gas discharge by at least an order of magnitude, 2) locating areas of significant gas discharge in an initial survey can inform areas of interest for *in-situ* measurements, and 3) detailed point measurements can be more confidently extrapolated to estimate vent field-scale gas flux. In a detailed study aimed at quantitative measurements of gas fluxes, automated image processing techniques applied to the local video imagery should be used to determine bubble parameters (rise rate, size, and fluxes). Automated processing would alleviate the need for bubble traps to measure gas flux. Due to the illustrative focus of our study and some difficulties with lighting and image quality (Section 4.4), we used manual methods here to demonstrate the potential benefits of data collected by the sensor suite over a small area. Coupled automated analysis of video data and high resolution, low-altitude ROV multibeam will yield estimates of gas discharge with lower uncertainty than other, ship-based methods, while still utilizing a relatively simple suite of sensors.

6.3 Application to Other Submarine Arc Volcanoes

Confirmed hydrothermal activity occurs at ~40% of submarine volcanoes along intra-oceanic and intracontinental arcs [*Baker et al.*, 2008; *Baker*, 2017; *de Ronde et al.*, 2005; *Resing et al.*, 2009]. Fluid and gas fluxes at these shallow hydrothermal sites are estimated to have a large impact on the global ocean [e.g., *Baker,* 2017]. Hydrothermal fluids in arc settings typically vent at shallower depths than those along mid-ocean ridges and are often more enriched in magmatic gases such as CO_2 and major elements including Fe, Mn, and Al [e.g, *Resing et al.,* 2009]. The shallow discharge depths and gas and chemical enrichment make fluid and gas discharge from arc systems especially important for the upper oceans. Indeed, shallow hydrothermal systems may seed Fe and S into the upper ocean, potentially enhancing the hydrothermal biosphere and increasing upper ocean primary productivity [*Hawkes et al.*, 2014; *Kelley et al.*, 2002]. Despite the potential impact of arc volcano hosted vent fields, many flux estimates for these hydrothermal systems are based upon CTD casts and tows of sensors in the water column. Few quantitative *in-situ* measurements of fluid flow and gas discharge exist. Future studies using ROV-based *in-situ* measurements of gas and fluid discharge from shallow arc-based hydrothermal systems would improve constraints on the importance of these systems by accurately quantifying flux estimates. The complementary use of the optical-acoustic methods presented here is particularly well-suited for such studies as it yields high-confidence flux estimates within a relatively short field period.

6.4 Future Work

Due to the often wide distribution of diffuse hydrothermal flow within a hydrothermal field, accurate field-scale flux estimates are difficult. Published estimates of the ratio of diffuse to focused heat fluxes at mid-ocean ridge hydrothermal fields varies from 0 to 1000 with many studies concluding that this ratio is probably ~5-10 for most sites [e.g., *Baker et al.,* 1993; *Barreyre et al.*, 2012; *Escartin et al.*, 2015; *German et al.,* 2010; *Ginster et al.*, 2004; *Mittelstaedt et al.* 2012; 2016; *Ramondenc et al.,* 2006; *Rona and Trivett,* 1992; *Stein and Fisher,* 2001; *Veirs et al.*, 2006]. Recent work improves the extrapolation of point measurements of diffuse venting to field-scales by using accurate photo mosaic maps of microbial distributions as proxies for the locations of active hydrothermal flow. Our results at Kick’em Jenny Volcano demonstrate that areas of active diffuse venting can be much smaller than areas covered by microbial mats. However, it is unclear if this holds true at deep, mid-ocean ridge hosted hydrothermal systems where fluid chemistry, ambient temperatures, and crustal permeability structure can differ from arc systems. Future work to quantify the distribution of microbial mats and active fluid flow at a mid-ocean ridge hosted hydrothermal site could resolve this question. These surveys will also benefit from recent advances in the structured light system that allow deployment on AUVs at higher altitudes (6 m) [*Smart and Roman*, 2017]. If differences between areas of active venting and microbial mats at deep-sea vents are similar to Kick'em Jenny, the global volume and heat flux of diffuse relative to focused venting could be much smaller than previously suggested.

7. CONCLUSIONS

This study at the Kick'em Jenny Volcano demonstrates a suite of complementary ROV-based acoustic and optical methods to accurately locate areas of active diffuse venting, microbial mats, and gas seeps (bubbles), and to measure diffuse effluent flow rates and gas seep bubble characteristics (rise rate, size). The methods employed to locate venting, bacteria, and bubble streams include use of a structured light laser system and a high-resolution, downward facing multibeam system. Local measurements analyze imagery of diffuse effluent and bubbles from a stereo pair of computer vision cameras.

Results from this study indicate that combining accurate locations of active diffuse venting or gas bubble streams with point measurements of fluid or gas fluxes reduces uncertainty in field-scale flux estimates. Accurate maps of the locations of active diffuse flow within the Kick'em Jenny crater yield estimates of diffuse fluxes up to 40 times less than if flow is assumed to occur in all areas covered by microbial mats. Using high-resolution multibeam data to locate bubble streams improves the number of resolvable bubble streams from ~1 m^{-2} to 10's m^{-2}. Combined, these methods provide an efficient, high confidence protocol for assessing diffuse venting and gas discharge.

We suggest that comprehensive flux studies at any marine hydrothermal system (arc or mid-ocean ridge) will benefit by use of a similar methodology for calculation of field-scale fluxes. Future work should determine if the differences in diffuse flux based upon mapped active venting or mapped microbial mats at Kick'em Jenny are similar at mid-ocean ridge hosted hydrothermal vents; if similar differences are observed, the global ratio of diffuse to focused hydrothermal venting could be much smaller than previously suggested.

8. ACKNOWLEDGEMENTS

The authors would like to thank the Ocean Exploration Trust, the captain and crew of the E/V *Nautilus*, chief shipboard scientist S. Carey, and the telepresence team of Inner Space Center at the University of Rhode Island for their indispensable help during the NA054 seagoing expedition. E.M would like to thank C. German for the opportunity to participate in the TREET project, as well as all the other TREET team members without whom this project would not have come to fruition. The authors would also like to acknowledge the Roman Lab at the University of Rhode Island for use of the imaging suite sensors. E.M. was funded by his start-up from the University of Idaho. Ship time was supported by NOAA grant number NA13OAR4600094 and the TREET project was funded by NSF grant #OCE-1344250. The authors declare that they have no competing interests.

.

9. REFERENCES CITED

Baker, E. T., G. Massoth, S. Walker, and R. W. Embley (1993), A method for quantitatively estimating diffuse and discrete hydrothermal discharge, *Earth Planet. Sci. Lett.*, *118*, 235-249.

Baker, E. T., R. M. Haymon, J. Resing, N. White, S. Walker, G. A. Macdonald, and E. Nakamura (2008), High-resolution surveys along the hot spot-affected Galapagos Spreading Center: 1. Distribution of hydrothermal activity, *Geochem. Geophys. Geosys.*, *9*(9), doi:10.1029/2008GC002028.

Baker, E. T. (2017), Exploring the ocean for hydrothermal venting: New techniques, new discoveries, new insights, *Ore Geology Reviews*, vol. 86, doi: 10.1016/j.oregeorev.2017.02.006.

Barreyre, T., J. Escartin, R. Garcia, M. Cannat, E. Mittelstaedt, and R. Prados (2012), Structure, temporal evolution, and heat flux estimates from the Lucky Strike deep-sea hydrothermal field derived from seafloor image mosaics, *Geochem. Geophys. Geosys.*, *13*(4), doi:10.1029/2011GC003990.

Barreyre, T., A. Davaille, E. Mittelstaedt, and C. Small (2015), A non-invasive method for estimating heat flux out of a hydrothermal crack derived from fluid dynamics analog modeling, AGU Fall Meeting Abstracts.edited by

Bell, K. C., M. L. Brennan, J. Flanders, N. Raineault, and K. Wagner (2016), Technology, Exploration Vessel Nautilus, *Oceanography*, *29*(1), 4-9.

Bell, K. L. C., C. R. German, Z. Mirmalek, and A. Pallant (2015), Transforming Remotely Conducted Research Through Ethnography, Education & Rapidly Evolving Technologies (TREET), *Oceanography*, *28*(1), 40-43.

Carey, S., R. Ballard, K. L. C. Bell, R. J. Bell, P. Connally, F. Dondin, S. Fuller, J. Gobin, P. Miloslavich, B. Phillips, C. Roman, B. Seibel, N. Siu, and C. Smart (2014a), Cold seeps associated with a submarine debris avalanche deposit at Kick'em Jenny Volcano, Grenada (Lesser Antilles), *Deep Sea Research Part I: Oceanographic Research Papers*, *93*, 156-160.

Carey, S., K. L. C. Bell, R. D. Ballard, C. Roman, F. Dondin, P. Miloslavich, J. Gobin, B. Seibel, R. Bell, C. Smart, S. A. Fuller, N. Siu, P. Connally, R. Blake, K. Wishner, and B. T. Phillips (2014b), Fluid/Gas Venting and Biological Communities at Kick'em Jenny Submarine Volcano, Grenada (West Indies), *Oceanography*, *27*(Supplement), 38-41.

Carey, S., K. L. Bell, C. Roman, F. Dondin, R. Robertson, J. Gobin, S. Wankel, A. P. Michel, D. J. Amon, and L. Marsh (2015), Exploring Kick'em Jenny Submarine Volcano and the Barbados Cold Seep Province, Southern Lesser Antilles *Oceanography*, *28*, 38-39.

Carey, S., R. Olsen, K. L. C. Bell, R. Ballard, F. Dondin, C. Roman, C. Smart, M. D. Lilley, J. E. Lupton, B. Seibel, W. Cornell, and C. Moyer (2016), Hydrothermal venting and mineralization in the crater of Kick'em Jenny submarine volcano, Grenada (Lesser Antilles), *Geochemistry Geophysics Geosystems (G3)*, *17*.

de Ronde, C. E., M. Hannington, P. Stoffers, I. Wright, R. Ditchburn, A. Reyes, E. Baker, G. Massoth, J. Lupton, and S. Walker (2005), Evolution of a submarine magmatic-hydrothermal system: Brothers volcano, southern Kermadec arc, New Zealand, *Economic Geology*, *100*(6), 1097-1133.

Devine, J. D., and H. Sigurdsson (1995), Petrology and eruption styles of Kick'em-Jenny submarine volcano, Lesser Antilles island arc, *Journal of volcanology and geothermal research*, *69*(1-2), 35-58.

Elderfield, H., and A. Schultz (1996), Mid-ocean ridge hydrothermal fluxes and the chemical composition of the ocean, *Annual Review of Earth and Planetary Science*, *24*, 191-224.

Escartin, J., T. Barreyre, M. Cannat, R. Garcia, N. Gracias, A. Deschamps, A. Salocchi, P.-M. Sarradin, and V. Ballu (2015), Hydrothermal activity along the slow-spreading Lucky Strike ridge segment (Mid-Atlantic Ridge): Distribution, heatflux, and geological controls, *Earth Planet. Sci. Lett.*, *431*, 173-185.

Fisher, A. T., and K. Becker (1991), Heat flow, hydrothermal circulation and basalt intrusions in the Guaymas Basin, Gulf of California, *Earth Planet. Sci. Lett.*, *103*, 84-99.

Fledermaus (2014), FMMidwater edited, Software.

German, C., A. M. Thurnherr, J. Knoery, J.-L. Charlou, P. Jean-Baptiste, and H. N. Edmonds (2010), Heat, volume and chemical fluxes from submarine venting: A synthesis of results from the Rainbow hydrothermal field 36°N MAR, *Deep-Sea Research 1*, *57*, 518-527.

Germanovich, L. N., R. S. Hurt, J. E. Smith, G. Genc, and R. P. Lowell (2015), Measuring fluid flow and heat output in seafloor hydrothermal environments, *J. Geophys. Res.*, doi:10.1002/2015JB012245.

Ginster, U., M. J. Mottl, and R. P. Von Herzen (1994), Heat flux from black smokers on the Endeavour and Cleft segments, Juan de Fuca Ridge, *J. Geophys. Res.*, *99*(B3), 4937-4950.

Glasby, G. P. (1971), Direct observations of columnar scattering associated with geothermal gas bubbling in the Bay of Plenty, New Zealand, *J. Mar. Freshw. Res.*, *5*, 483-496.

Graff, J. R., J. A. Blake, and K. F. Wishner (2008), A new species of Malacoceros (Polychaeta: Spionidae) from Kick'em Jenny, a hydrothermally active submarine volcano in the Lesser Antilles Arc, *Journal of the Marine Biological Association of the UK*, *88*(05), 925-930.

Hawkes, J. A., D. P. Connelly, M. J. Rijkenberg, and E. P. Achterberg (2014), The importance of shallow hydrothermal island arc systems in ocean biogeochemistry, *Geophys. Res. Lett.*, *41*(3), 942-947.

Inglis, G., C. Smart, J. Vaughn, and C. Roman (2012), A Pipeline for Structured Light Bathymetric Mapping, in *Intelligent Robots and Systems, Proceedings. October 7-12, IEEE/RSJ International Conference on*, edited.

Kelley, D. S., J. A. Baross, and J. R. Delaney (2002), Volcanoes, fluids, and life in submarine environments, *Annual Review of Earth and Planetary Science*, *30*, 385-491.

Lindsay, J. M., J. B. Shepherd, and D. Wilson (2005), Volcanic and scientific activity at Kickâ€™em Jenny submarine volcano 2001â€“2002: implications for volcanic hazard in the southern Grenadines, Lesser Antilles, *Natural Hazards*, *34*(1), 1-24.

Lutz, R. A., T. M. Shank, G. W. I. Luther, C. Vetriani, M. Tolstoy, D. B. Nuzzio, T. S. Moore, F. Waldhauser, M. Crespo-Medina, A. D. Chatziefthimiou, E. R. Annis, and A. J. Reed (2008), Interrelationships between vent fluid chemistry, temperature, seismic activity, and biological community structure at a mussel-dominated, deep-sea hydrothermal vetn along the East Pacific Rise, *Journal of Shellfish Research*, *27*(1), 177-190.

Merewether, R., M. S. Olsson, and P. Lonsdale (1985), Acoustically detected hydrocarbon plumes rising from 2-km depths in Guaymas Basin, Gulf of California, *Journal of Geophysical Research: Solid Earth*, *90*(B4), 3075-3085.

Mittelstaedt, A. Davaille, P. E. van Keken, N. Gracias, and J. Escartin (2010), A noninvasive method for measuring the velocity of diffuse hydrothermal flow by tracking moving refractive index anomalies, *Geochem. Geophys. Geosys.*, *11*(10), doi:10.1029/2010GC003227.

Mittelstaedt, J. Escartin, N. Gracias, J.-A. Olive, T. Barreyre, A. Davaille, M. Cannat, and R. Garcia (2012), Diffuse versus discrete venting at the Tour Eiffel vent site, Lucky Strike hydrothermal field, Geochem. Geophys. Geosys., 13(4), doi:10.1029/2011GC003991.

Mittelstaedt, E., T. Crone, D. Fornari, J. Kinsey, D. S. Kelley, and M. Elend (2016), Diffuse venting at the ASHES hydrothermal field: Heat flux and tidally modulated flow variability derived from in situ time-series measurements, *Geochem. Geophys. Geosys.*, *17*, doi: 10.1002/2015GC006144.

Moore, T. S., T. M. Shank, D. B. Nuzzio, and G. W. I. Luther (2009), Time-series chemical and temperature habitat characterization of diffuse flow hydrothermal sites at 9º50'N East Pacific Rise, *Deep-Sea Research II*, *56*, 1616-1621.

Morton, B. R., G. Taylor, and J. S. Turner (1956), Turbulent gravitational convection from maintained and instantaneous sources, *Proceedings of the Royal Society of London*, *234*, 1-23.

Nees, H. A., T. S. Moore, K. M. Mullaugh, R. R. Holyoke, C. P. Janzen, S. Ma, E. Metzger, T. J. Waite, M. Yucel, and R. A. Lutz (2008), Hydrothermal vent mussel habitat chemistry, pre- and post-eruption at 9o50 North on the East Pacific Rise, *Journal of Shellfish Research*, *27*(1), 169-175.

Nikolovska, A., H. Sahling, and G. Bohrmann (2008), Hydroacoustic methodology for detection, localization, and quantification of gas bubbles rising from the seafloor at gas seeps from the eastern Black Sea, *Geochemistry Geophysics Geosystems (G3)*, *9*(10), 1-13.

Pruis, M. J., and H. P. Johnson (2004), Tapping into the sub-seafloor: examining diffuse flow and temperature from an active seamount on the Juan de Fuca Ridge, *Earth Planet. Sci. Lett.*, *217*, 379-388.

Ramondenc, P., L. N. Germanovich, K. L. Von Damm, and R. P. Lowell (2006), The first measurements of hydrothermal heat output at 9°50'N, East Pacific Rise, *Earth Planet. Sci. Lett.*, *245*, 487-497.

Resing, J. A., E. T. Baker, J. E. Lupton, S. L. Walker, D. A. Butterfield, G. J. Massoth, and K. i. Nakamura (2009), Chemistry of hydrothermal plumes above submarine volcanoes of the Mariana Arc, *Geochemistry, Geophysics, Geosystems*, *10*(2).

Roman, C., G. Inglis, J. I. Vaughn, C. Smart, B. Douillard, and S. Williams (2012), The Development of High-Resolution Seafloor Mapping Techniques, *Oceanography*, *25(1)*(supplement).

Rona, P., D. Jackson, T. Wen, C. Jones, K. Mitsuzawa, K. Bemis, and J. Dworski (1997), Acoustic mapping of diffuse flow at a seafloor hydrothermal site: Monolith Vent, Juan de Fuca Ridge, *Geophys. Res. Lett.*, *24*(19), 2351-2354.

Rona, P. A., and D. A. Trivett (1992), Discrete and diffuse heat transfer at ASHES vent field, Axial Volcano, Juan de Fuca Ridge, *Earth Planet. Sci. Lett.*, *109*, 57-71.

Santana-Casiano, J. M., E. Fraile-Nuez, M. Gonzalez-Davila, E. T. Baker, J. A. Resing, and S. Walker (2016), Significant discharge of CO2 from hydrothermalism associated with the submarine volcano of El Hierro Island, *Scientific Reports*, *6*(25686), doi:10.1038/srep25686.

Schmidt, C., R. Vuillemin, C. L. Le Gall, F. Gaill, and N. Le Bris (2008), Geochemical energy sources for microbial primary production in the environment of hydrothermal vent shrimps, *Mar. Chem.*, *108*, 18-31.

Schneider von Deimling, J., and C. Papenberg (2012), Technical Note: Detection of gas bubble leakage via correlation of water column multibeam images, *Ocean Science*, *8*(2), 175--181.

Schultz, A., J. R. Delaney, and R. E. McDuff (1992), On the partitioning of heat flux between diffuse and point source seafloor venting, *J. Geophys. Res.*, *97*(B9), 12299-12314.

Skarke, A., C. Ruppel, M. Kodis, D. Brothers, and E. Lobecker (2014), Widespread methane leakage from the sea floor on the northern US Atlantic margin, *Nature Geoscience Letters*, *7*, 657-661.

Smart, C., C. Roman, and S. Carey (2017), Detection of diffuse seafloor venting using a strucutred light laser sensor: 1. Development of a classification based detection method, *Earth and Space Sciences*, 4, 348–363, doi:10.1002/2017EA000262.

Smart, C., and C. Roman (2017), Detection of diffuse seafloor venting using a structured light laser sensor: 2. Evaluation of detection sensitivity and limitations, *Earth and Space Science*, 4, 364–376, doi:10.1002/2017EA000263.

Smart, C. J., C. Roman, and S. N. Carey (2013), Detection of diffuse seafloor venting using structured light imaging, *Geochemistry, Geophysics, Geosystems*, *14*(11), 4743--4757.

Socolofsky, S. A., J. A. Breier, J. S. Seewald, B. Wang, S. Maness, C. Nygren, and N. Raineault (2015), Fate and Transport of Gas Bubbles from Natural Seeps in the Northern Gulf of Mexico, *Oceanography*, *28*(1, Supplement).

Spiess, F. N., K. C. Macdonald, T. Atwater, R. Ballard, A. Carranza, D. Cordoba, V. Cox, M. Diaz Garcia, J. Francheteau, J. Guerrero, J. Hawkins, R. M. Haymon, R. Hessler, T. Juteau, M. Kastner, R. Larson, B. P. Luyendyk, J. D. Macdougall, S. P. Miller, W. Normark, J. A. Orcutt, and C. Rangin (1980), East Pacific Rise: Hotsprings and Geophysical Experiments, *Science*, *207*(4438), 1421-1433.

Stein, C. A., and S. Stein (1994), Constraints on hydrothermal heat flux through the oceanic lithosphere from global heat flow *J. Geophys. Res.*, *99*, 3081-3095.

Stein, J. S., and A. T. Fisher (2001), Multiple scales of hydrothermal circulation in Middle Valley, northern Juan de Fuca Ridge: Physical constraints on geological models, *J. Geophys. Res.*, *106*(B5), 8563-8580.

Stewart, F. J., I. L. G. Newton, and C. M. Cavanaugh (2005), Chemosynthetic endosymbioses: Adaptations to oxic-anoxic interfaces, *Trends in Microbiology*, *13*(9), 439-448.

Trivett, D. A., and A. J. I. Williams (1994), Effluent from diffuse hydrothermal venting 2. Measurements of plumes from diffuse hydrothermal vents at the southern Juan de Fuca Ridge, *J. Geophys. Res.*, *99*(C9), 18417-18432.

Urban, P., K. Köser, and J. Greinert (2017), Processing of multibeam water column image data for automated bubble/seep detection and repeated mapping, *Limnology and Oceanography: Methods*, *15*(1), 1--21.

Veirs, S. R., R. E. McDuff, and F. R. Stahr (2006), Magnitude and variance of near-bottom horizontal heat flux at the Main Endeavour hydrothermal vent field, *Geochem. Geophys. Geosys.*, *7*(2), doi:10.1029/2005GC000952.

Von Damm, K. L. (1990), Seafloor hydrothermal activity: Black smoker chemistry and chimneys, *Annual Review of Earth and Planetary Science*, *18*, 173-204.

Von Damm, K. L., S. E. Oosting, R. Kozlowski, L. G. Buttermore, D. C. Colodner, H. N. Edmonds, J. M. Edmond, and J. M. Grebmeier (1995), Evolution of East Pacific Rise hydrothermal vent fluids following a volcanic eruption, *Nature*, *375*, 47-50.

Von Damm, K. L., and M. Lilley (2004), Diffuse flow hydrothermal fluids from 9°50'N East Pacific Rise: Origin, evolution and biogeochemical controls, in *The Subseafloor Biosphere at Mid-Ocean Ridges*, edited by W. S. D. Wilcock, et al., American Geophysical Union, Washington D.C.

Wang, B., S. A. Socolofsky, J. A. Breier, and J. S. Seewald (2016), Observations of bubbles in natural seep flares at MC 118 and GC 600 using in situ quantitative imaging, *Journal of Geophysical Research: Oceans*, *121*(4), 2203-2230, doi:10.1002/2015JC011452.

Wang, B., and S. A. Socolofsky (2015), A deep-sea, high-speed, stereoscopic imaging system for in situ measurement of natural seep bubble and droplet characteristics, *Deep Sea Research Part I: Oceanographic Research Papers*, *104*, 134 - 148.

Watlington, R. A., W. D. Wilson, W. E. Johns, and C. Nelson (2002), Updated bathymetric survey of Kick-'em-Jenny submarine volcano, *Marine Geophysical Researches*, *23*, 271-276.

Weber, T. C., L. Mayer, J. Beaudoin, K. Jerram, M. Malik, B. Shedd, and G. Rice (2012), Mapping Gas Seeps with the Deepwater Multibeam Echosounder on Okeanos Explorer, *Oceanography*, *25*(1, Supplement), 54-55.

Westerweel, J. (1997), Fundamentals of digital particle image velocimetry, *Measurement science and technology*, *8*(12), 1379.

Willert, C. E., and M. Gharib (1991), Digital particle image velocimetry, *Exp Fluids*, *10*(181-193).

Wishner, K., J. R. Graff, J. W. Martin, S. Carey, H. Sigurdsson, and B. A. Seibel (2005), Are midwater shrimp trapped in the craters of submarine volcanoes by hydrothermal venting?, *Deep Sea Research Part I: Oceanographic Research Papers*, *52*, 1528-1535.

10. FIGURE CAPTIONS

Figure 1. Kick'em Jenny volcano is located ~8 km northwest of Grenada within the Lesser Antilles Arc. The volcano summit reaches ~180 m below sea level and hosts a (inset) ~100 m deep crater with a several meter deep inner crater, within which active hydrothermal systems serve as the basis for this study.

Figure 2. The Shrimp Vent area is defined by rising bubbles and areas of diffuse flow which support biota including bacteria and shrimp. (A) ROV Hercules collects samples within the shrimp vent area, the steep hillside is apparent and numerous, closely spaced rising bubble streams are visible. (B) Shrimp live amongst diffuse flow and microbial mats within crevices in rust-colored rock.

Figure 3. The inner crater at Kick'em Jenny was surveyed using the high resolution imaging suite. The resulting photo mosaics provides a comprehensive overview of the area including changes in sediment and microbial mats. (upper right) Champagne Vent and the (lower right) Shrimp Vent area are indicated and enlarged.

Figure 4. Rising bubble streams and hydrothermal fluids were imaged by the forward looking mono stereo cameras to allow image processing for bubble rise rate and size and fluid velocities. (A) The ROV arm holds the white background board behind rising bubbles during (C) image acquisition by the stereo cameras. (B) Similarly, the speckled background board is held behind rising fluid flow during (D) image acquisition by one of the same stereo cameras.

Figure 5. A drawing of the ROV *Hercules* denoting the locations of the high resolution imaging sensor package mounted on the back of the vehicle, which includes downward looking stereo cameras, a 1350kHz multibeam sonar, and a structured light camera. The imaging domains of each sensor are shown as shaded fields and (inset) a cartoon of laser and sonar data are shown. A stereo pair of computer vision cameras are located on the front *Hercules* for imaging of diffuse effluent and bubble streams

Figure 6. Navigation corresponding to the high resolution imaging surveys conducted at Champagne (blue) and Shrimp Vent (red) are shown. Additionally, areas of bubble imaging, flow imaging and bubble trap sampling are indicated by green, orange and gray circles respectively. Each circle corresponds to the location of the front of the vehicle during sampling and frequently multiple samples were collected at nearby sites by moving the ROV manipulator.

Figure 7. Bubble flux values were determined by collecting rising bubbles from several individual gas seeps at Champagne Vent and Shrimp Vent. (A) Bubble discharge at the Champagne vent occurred at a primary, high flux seep and numerous other seeps with relatively similar bubble fluxes. (B) The ROV manipulator held the bubble trap container (35cm diameter and a 2 liter capacity) in place over each bubble stream.

Figure 8. A raw image of from the structured light laser system shows a crisp laser line (right) which becomes blurred (left) as the sheet laser interacts with turbulent density anomalies (e.g., active venting). The laser line is extracted from the raw images and the laser line distortion is detected, serving as a proxy for detection of active fluid flow and changes in seafloor cover.

Figure 9. Using a machine classification routine, the (B) optical intensity of a laser image and the intensity weighted second moment of the laser line are used to determine areas of (C) seafloor, microbial mats, and active venting within a given area (A – photo mosaic near Shrimp vent).

Figure 10. (A) Large impedance contrasts between rising bubbles and water produce significant returns in the 1350 kHz multibeam sonar water column data. In the image shown, the three rising bubble streams are apparent above the seafloor return. (B) Locations of rising bubble streams from picks in multibeam sonar water column data are converted to X,Y values (black dots). Pick separated by <30 cm in X and 5 cm in Y are considered to be the same bubble stream (red circles). (C) High densities of bubble streams (up to 56 streams m^{-2}) are observed around Shrimp and Champagne vents.

Figure 11. Areas of turbulent density anomalies are detected at (A, B, C) Shrimp Vent and (D, E, F) Champagne vent using the structured light laser sensor. Shrimp vent is dominated by microbial mats while active fluid flow is discrete and isolated. (A) The color photo mosaic provides an overview of the site with visible white microbial mats. (B) Classification results showing detected seafloor, bacteria, and active venting. (C) The same data is presented as in (B) however only areas of active venting are shown. (D, E, F) Similar figures are shown for the area around Champagne Vent. Within the classification figures (E, F) a small amount of venting is detected at 50.2 m, 142.5 m, however, when referencing the mosaic it is apparent that this is a false positive due to disturbance of fine sediment by a nearby fish (apparent in D). It is likely that the majority of active fluid flow is located on the main mound.

Figure 12. Diffuse Flow Velocimetry is used to determine the flow rates of diffuse effluent rising in front of (A) a speckled background board. (B) Time averaged velocities (arrows in A and B) show patterns of higher and lower vertical velocities (contours) across the background board. (C) Spatial medians taken from each DFV calculation (red dots) indicate a relative constant upwelling rate (~1.5 cm/s) from this diffuse vent. A ten-point-wide running average is also shown (blue line).

Figure 13. Median vertical velocities (black dots) measured by DFV increase approximately as the square-root of fluid temperature anomaly as predicted for turbulent jets [*Morton,* 1956]. Vertical bars indicate estimated errors in flow rates based upon the standard deviations in spatial median flow rates.

Figure 14. Stereo imagery of bubble streams was processed manually to measure (top) rise rates and (bottom) volumes of bubbles. A weak linear decrease in rise rates with increasing bubble size is found suggesting that drag forces likely slow larger bubbles.

10. TABLES

Table 1. Bubble Flux Measurements

Sample Number	Vent Location	Two Liter fill time (min)	Liters/Minute
1	Champagne Vent 1	11:40	0.171
2	Champagne Vent 1	11:10	0.179
3	Champagne Vent 1	11:20	0.176
4	Champagne Vent 2	1:00	2
5	Champagne Vent 2	1:00	2
6	Champagne Vent 2	0:59	2.03
7	Shrimp Vent 1	4:36	0.435
8	Shrimp Vent 1	4:24	0.455
9	Shrimp Vent 1	4:06	0.488
10	Shrimp Vent 2	4:16	0.469
11	Shrimp Vent 2	4:12	0.476
12	Shrimp Vent 2	4:47	0.418

Table 2. Video Data and Processing Parameters

Survey Date	Survey Number	Vent Area	Number of Frames	Elapsed Time (s)	PIV Window Size (max:min)	DFV Window Size
26-Sep-14	1037	Shrimp	2306	230.6	32:8	24
26-Sep-14	1751	Champagne	2317	231.7	32:8	16
26-Sep-14	1816	Champagne	3770	377	32:8	16
26-Sep-14	1829	Champagne	3998	399.8	32:8	16
29-Sep-14	2340	north inner crater	3499	349.9	32:8	16
8-Oct-14	1928	linear crack	100	10	32:8	32

Table 3. Video Data and Processing Parameters

Survey Number	Median Vertical Velocity (cm/s)	Standard Deviation (cm/s)	Mean Exit Fluid Temperature (°C)	Temperature (°C) at height of DFV
1037	0.30	0.26	16.6	No data
1751	1.93	0.69	32.9	No data
1816	0.81	0.87	29	No data
1829	0.76	0.68	24.8	15.3
2340	1.40	0.20	26.7	20.6
1928	2.52	1.38	No data	50.8

Table 4. Structured Light Classification Results

Vent Site	Total Area* (m^2)	Bacteria (m^2)	Venting (m^2)	Seafloor (m^2)
Shrimp	222.3	14.8	0.35	179
Champagne	74.2	30.41	1.03	38.8

*Area of laser values are not always equal to the total successfully classified areas

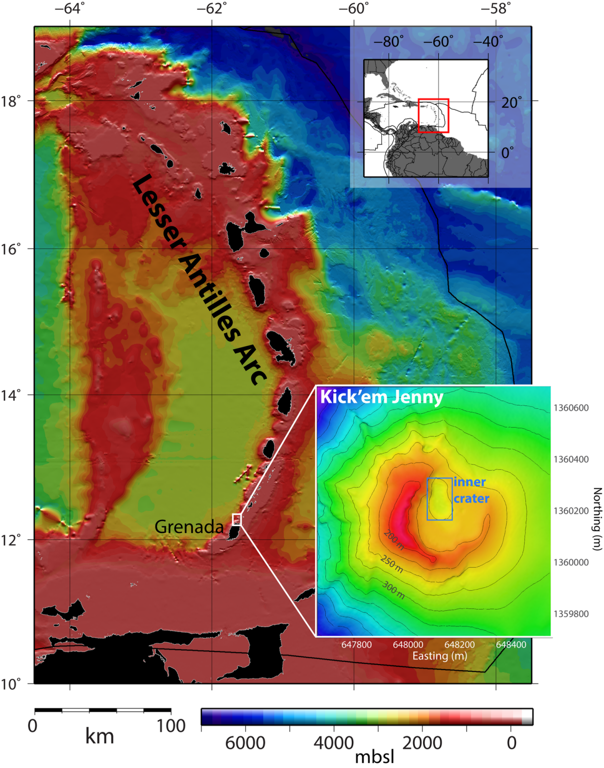

−64˚
−62˚
−60˚
−58˚
18˚
16˚
14˚
12˚
10˚
−80˚
−60˚
−40˚
20˚
0˚
Lesser Antilles Arc
Grenada
Kick'em Jenny
inner crater
200 m
250 m
300 m
1360600
1360400
1360200
1360000
1359800
Northing (m)
647800
648000
648200
648400
Easting (m)
0
km
100
6000
4000
2000
0
mbsl

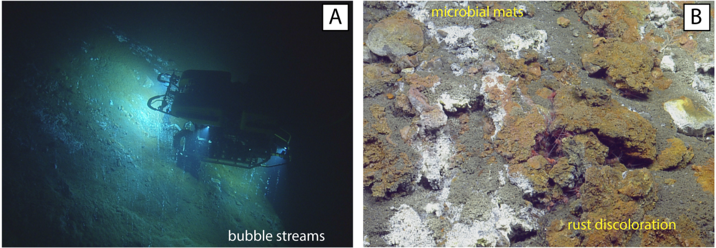
A
bubble streams
B
microbial mats
rust discoloration

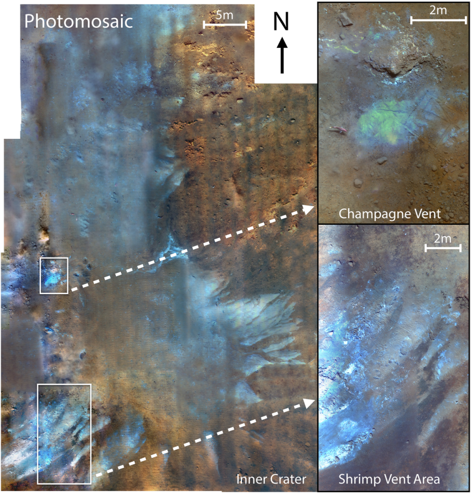

Photomosaic
5m
N
2m
Champagne Vent
2m
Inner Crater
Shrimp Vent Area

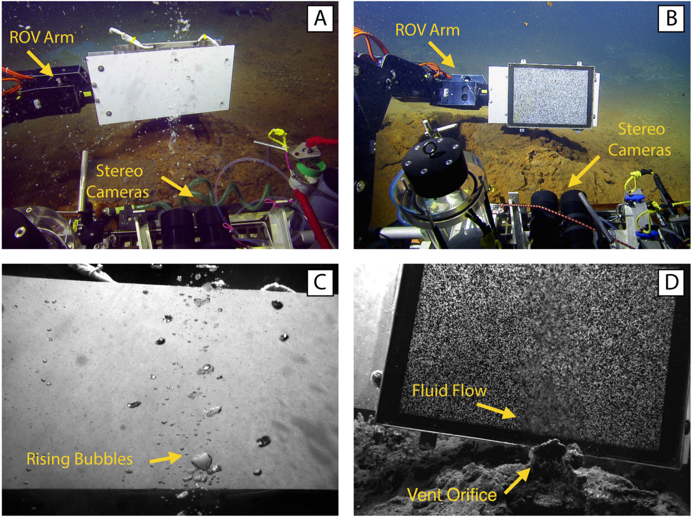
A
ROV Arm
Stereo
Cameras
B
ROV Arm
Stereo
Cameras
C
Rising Bubbles
D
Fluid Flow
Vent Orifice

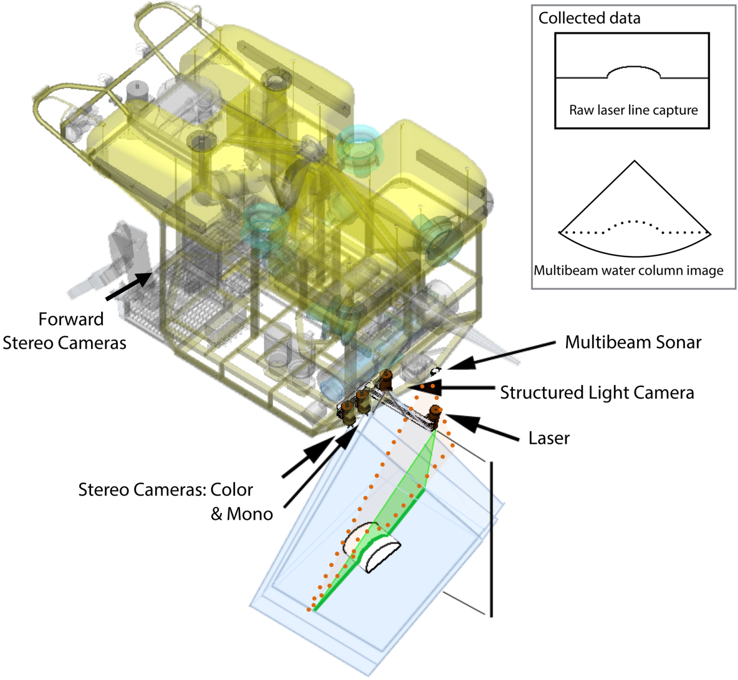

Collected data
Raw laser line capture
Multibeam water column image
Forward
Stereo Cameras
Multibeam Sonar
Structured Light Camera
Laser
Stereo Cameras: Color
& Mono

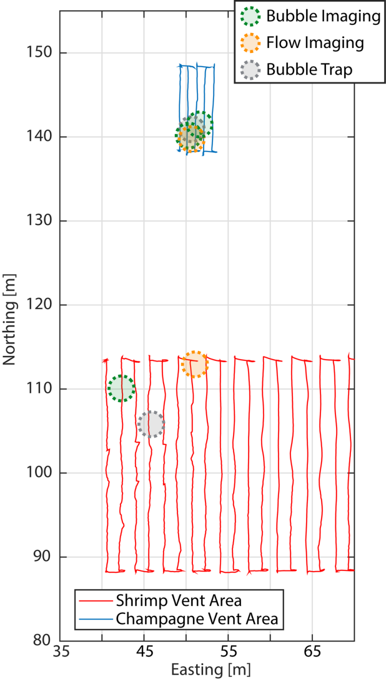

Bubble Imaging
Flow Imaging
Bubble Trap
Northing [m]
150
140
130
120
110
100
90
80
35
45
55
65
Easting [m]
Shrimp Vent Area
Champagne Vent Area

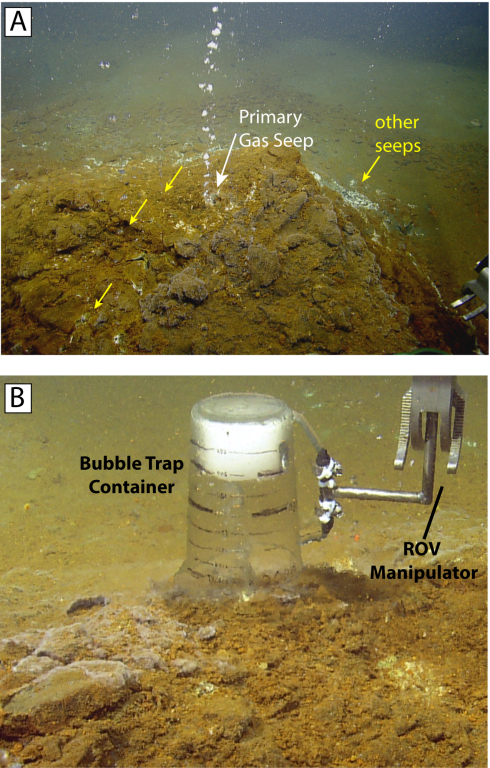
A
Primary
Gas Seep
other
seeps
B
Bubble Trap
Container
ROV
Manipulator

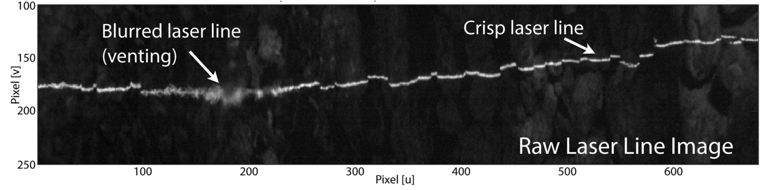
Blurred laser line
(venting)
Crisp laser line
Raw Laser Line Image
Pixel [v]
Pixel [u]
100
150
200
250
100
200
300
400
500
600

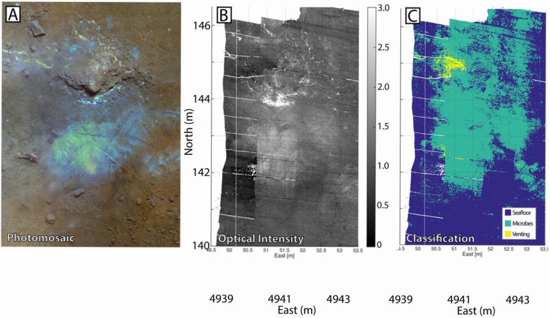
A
Photomosaic
B
Optical Intensity
146
144
142
140
North (m)
3.0
2.5
2.0
1.5
1.0
0.5
0
C
Classification
Seafloor
Microbes
Venting
4939
4941
4943
East (m)
4939
4941
4943
East (m)

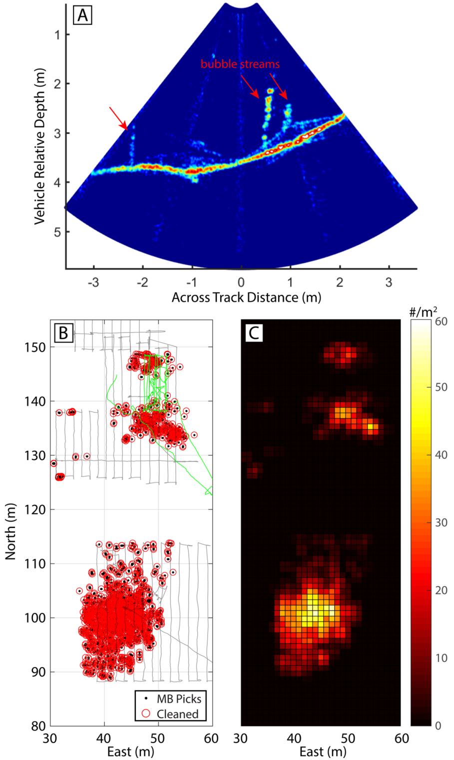
A
bubble streams
Vehicle Relative Depth (m)
Across Track Distance (m)
B
MB Picks
Cleaned
North (m)
East (m)
C
#/m²
East (m)

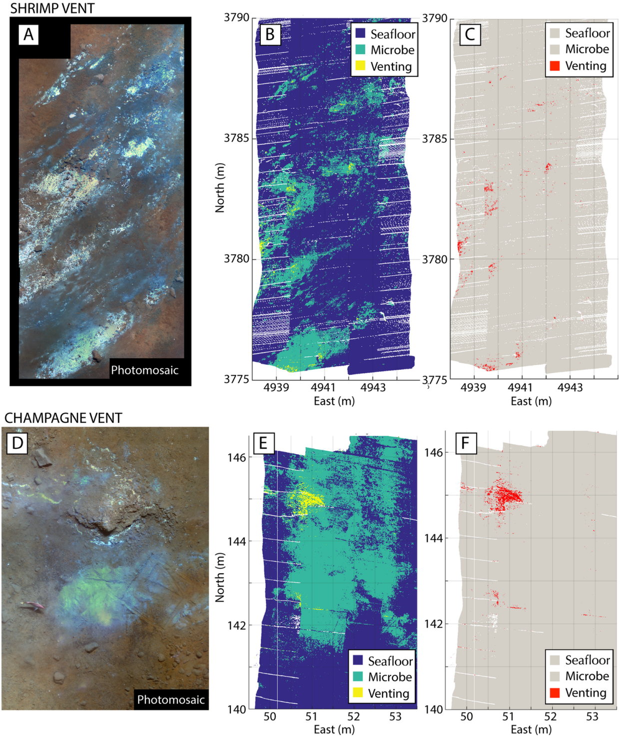

SHRIMP VENT
A
Photomosaic
B
Seafloor
Microbe
Venting
C
Seafloor
Microbe
Venting
3790
3785
3780
3775
North (m)
4939
4941
4943
East (m)
CHAMPAGNE VENT
D
Photomosaic
E
F
146
144
142
140
50
51
52
53

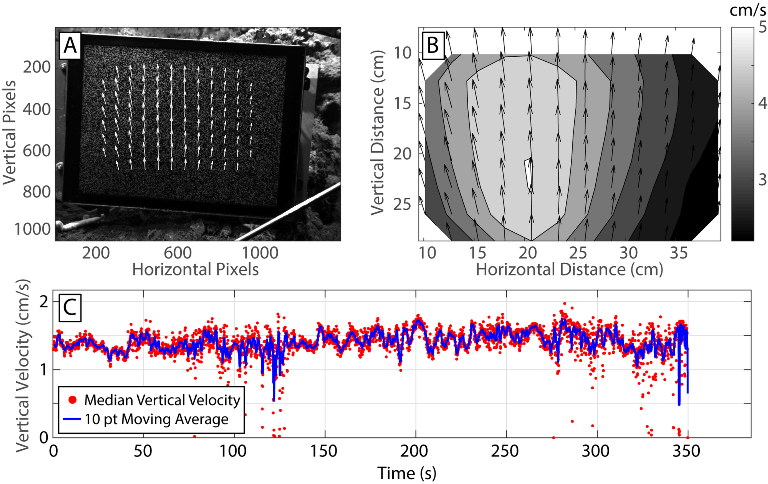

A
Vertical Pixels
200
400
600
800
1000
200
600
1000
Horizontal Pixels
B
cm/s
5
4
3
Vertical Distance (cm)
10
15
20
25
10
15
20
25
30
35
Horizontal Distance (cm)
C
Vertical Velocity (cm/s)
2
1
0
Median Vertical Velocity
10 pt Moving Average
0
50
100
150
200
250
300
350
Time (s)

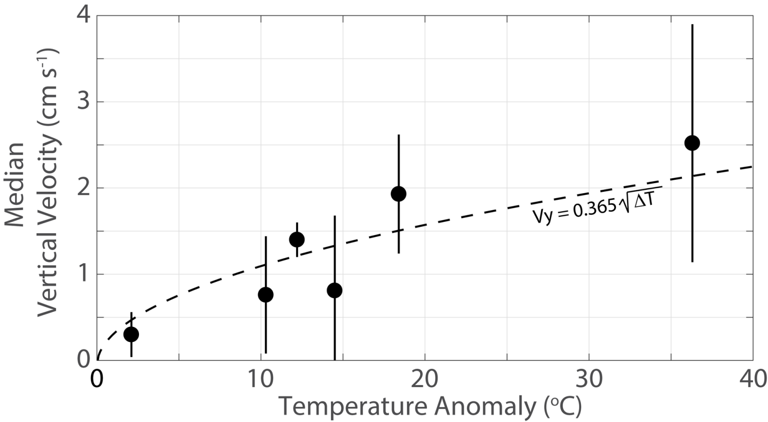
Median
Vertical Velocity (cm s-1)
Temperature Anomaly (oC)
Vy = 0.365√ΔT
0
1
2
3
4
0
10
20
30
40

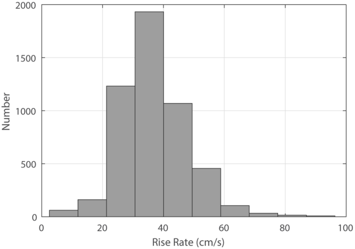

2000
1500
1000
500
0
Number
0
20
40
60
80
100
Rise Rate (cm/s)

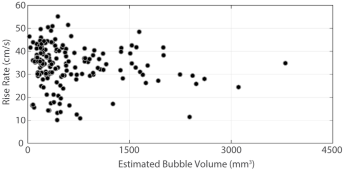

60
50
40
30
20
10
0
Rise Rate (cm/s)
0
1500
3000
4500
Estimated Bubble Volume (mm³)